Diego Mercerat and Dylan Mikesell
*Earth, Planets and Space* (2023) 75:31
https://doi.org/10.1186/s40623-023-01785-9

Earth, Planets and Space

FULL PAPER

Open Access

# A look at the blind Kumamoto experiment: combining active and passive seismic observations to avoid Rayleigh-wave mode misidentification

E. Diego Mercerat[1*] and T. Dylan Mikesell[2]

**Abstract**

We present our pathway through participation in the blind Kumamoto exercise, particularly the Step 1 of site characterization. The combination of passive and active seismic imaging techniques is used to image the velocity profile beneath the KUMA site. The estimation of the broadband Rayleigh wave dispersion curve is based on cross-correlations of ambient seismic noise and analysis of active seismic shots. We calculate correlations from the entire time series (only vertical components) of each seismic array after classical pre-processing of ambient noise data. Then, a passive seismic section is constructed using all available stations pairs and stacking the cross-correlation traces with similar interstation distances. The obtained passive seismic section is analyzed using a high-resolution Radon transform to obtain the dispersion image of Rayleigh waves traveling through the KUM-LL, KUM-M and KUM-SM arrays. Then, the information is merged and interpolated to obtain the final broadband dispersion curve. In addition, active source seismic data are used with the high-resolution Radon technique to constrain the model at shallow depths (< 30 m). Then, a broadband dispersion image is constructed with significant energy from 0.9 Hz to 45 Hz. The final dispersion curve is inverted using the non-linear neighborhood algorithm. Using just the fundamental mode Rayleigh wave, a first model with normal velocity variation in depth is obtained that corresponds well with the preferred model provided by the organizing committee. The addition of a mHVSR curve in a joint inversion better constrains the deeper part of the model (> 1 km). After comparison of the submitted dispersion curve to the theoretical dispersion curve for the preferred model (Step 4 of the blind test), the authors note that there was a clear misinterpretation in the fundamental mode of their submitted results, especially at frequencies higher than 5 Hz. Using both fundamental (only visible in the passive data set) and first overtones of Rayleigh waves (only visible in the active seismic data set) a refined velocity model could have been inferred, but we decided to keep our first submitted result. This detailed interpretation should be further studied as dispersion images from forward and backward hammer shots are quite different, which may indicate strong variations in the geometry and/or shear-wave velocities of the first meters of the subsurface.

**Keywords** Seismic interferometry, Ambient noise, Site characterization, Surface waves

*Correspondence:
E. Diego Mercerat
diego.mercerat@cerema.fr
Full list of author information is available at the end of the article

**Graphical Abstract**

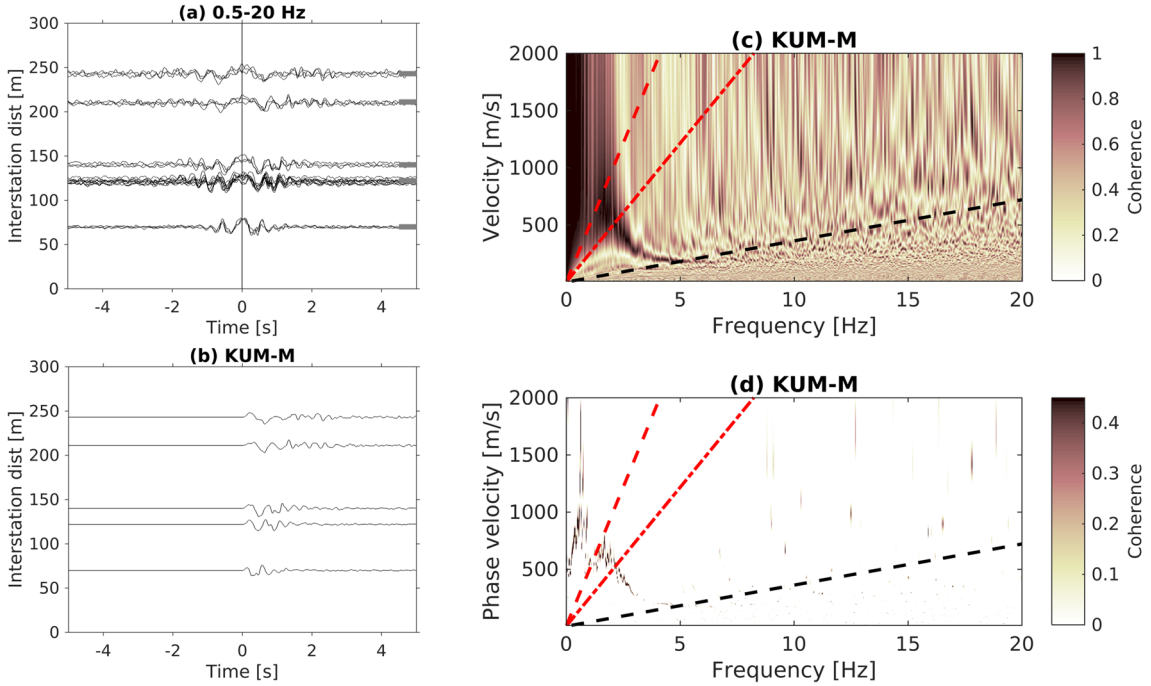


## Introduction

Microtremor array methods are used to extract information about subsurface geological structure from ambient seismic vibrations. These so-called ambient seismic vibrations (or noise) must be measured synchronously at the different stations within the array. A popular technique to extract subsurface information relies on a noise cross-correlation technique and is becoming widely adopted within the geophysical and earthquake engineering communities. The technique has been proven by several applications in different areas of the world and in different geological environments, from global to regional scales, and even at local scales (e.g., Shapiro et al. 2005; Bensen et al. 2007). Ambient noise cross-correlation studies in urban environments have also been used to obtain the geometry of the bedrock-sediment interface, as well as shear wave velocity profiles of the sedimentary layers within densely populated cities located in sedimentary basins (Saygin et al. 2016, Ma and Clayton 2016, Vassallo et al. 2019, Pacheco et al. 2022). Many of the previous ambient noise studies used data from temporary seismological networks, specifically deployed for characterization of the seismic response of each city in the framework of seismic hazard studies.

Here we propose to apply similar techniques to the microtremor data set for the blind site characterization exercise in the Kumamoto plain, Japan. The blind test organizing committee has provided the participant teams several ambient noise array observations carried out in the Kumamoto city center, around the KUMA site. The arrays were designed for classical FK-based and/or SPAC-based techniques (see Garofalo et al. 2016; Foti et al. 2018 for reviews of a similar blind exercise to benchmark different techniques). The main drawback of the ambient noise cross-correlation technique is the fact that ubiquitous and persistent noise sources, generally ocean generated, are relatively low frequency (< 1 Hz). Urban generated noise sources such as traffic, wind on buildings or trees, and other vibration sources, excite higher seismic frequencies (between 1 and 20 Hz) that in turn are not well-correlated over large distances. However, for short distances (< 1 km) they may still observe coherent behavior up to tens of Hertz in urban environments (Díaz et al. 2017). To counter the high-frequency deficiency of the cross-correlated noise traces, we combine the ambient noise cross-correlation analysis with active seismic data. The active seismic data from hammer shots can be used to estimate the high-frequency portion of the surface wave phase-velocity spectrum using standard techniques, such as multichannel analysis of surface waves (MASW, Park et al. 1999).

The data were collected by the local organizing committee of ESG6 and contains surface recordings of ambient noise in nested-triangular arrays for microtremor measurements (see Figure 1) and in-line arrays for active source measurement with varying inter-receiver spacings. A detailed summary of the data set is found in the companion paper by the organizing committee in this special number (Matsushima et al. 2022; Chimoto et al. 2022). In the following sections we present the a-priori knowledge of the field conditions available from the literature, as well as summarize the methods used in our analysis. The techniques presented in this work merge data from different arrays to significantly increase the usable frequency band to gain depth resolution in the investigation. Dispersion analysis of surface waves is done by direct picking in the phase velocity vs frequency dispersion images. Other studies have proposed similar approaches using group velocity dispersion curves, but their determination requires extra care about filtering in different frequency bands to pick envelope maxima (Pastén et al. 2016). In addition, we demonstrate that the combination of the phase velocity information with the horizontal-to-vertical spectral ratio (HVSR) data provides more accurate results of deeper velocity contrasts that are invisible when only considering the dispersion information. Finally, we discuss the inversion algorithm and operations used to estimate the shear-wave velocity profile. We interpret the resulting shear-wave velocity profile in terms of addition information obtained by combining both active and passive seismic data sets, and we compare our results to the "preferred model" provided by the organizers and the average dispersion curve from all participants in the blind study.

#### Kumamoto site

The Kumamoto site under investigation here is located within the Kumamoto plain, a sedimentary basin 22 km long and 8 km wide located in southwestern Japan. The plain is surrounded by the volcanoes Mount Kinbo and Mount Aso. Two rivers, Shirakawa and Midorikawa, cut through Kumamoto city and empty into the Ariake sea in western Japan. In terms of geology, the plain is composed of alluvial deposits, andesites, and pyroclastic flow deposits (Tsuno et al. 2017). The site is located in downtown Kumamoto, close to the strong motion station KUMA, situated at 32.77 N, 130.69 E at an elevation of 9.4 m above sea level.

From borings of the nearby KiK-net station KMMH16 (Chimoto et al. 2016), located 12 km to the east of the KUMA site, the geological column is composed by sandy deposits, intercalated by volcanic ash and tuff layers. The bedrock depth is estimated to be 600 m or more. Chimoto et al. (2016) estimate from microtremor observations that the soil column in the Mashiki town region, located to the east of the Kumamoto plain, less than 1 km from the KMMH16 KiK-net station, is composed of two sedimentary layers with shear wave velocities Vs = 100–150 m/s of very low surface thickness and Vs = 200–300 m/s with a depth not exceeding 30 m. This second layer lies over a layer of stiffer material considered as the "engineering bedrock" and having a Vs = 500 m/s. From these previous studies, the bedrock depth of the basin is expected to be greater than 400–500 m in the Kumamoto area.

#### Dispersion image estimation

Multichannel analysis of surface waves (MASW) is an array-based data processing method used to extract phase velocity dispersion information from Rayleigh and Love waves (e.g., Song et al. 1989). The basic idea is that one transforms the data recorded in the time-offset domain ($t-x$) to the frequency–velocity domain ($f-v$) to estimate the phase velocity at each frequency. This transform can take many forms. Shen et al. (2015) present an overview of the different methods and compare the resolution in each. One of the preferred transform methods is the $\tau-p$ transform, also known as the linear Radon transform (Trad et al. 2003 and the references therein). The High-Resolution Linear Radon Transform (HRLRT) was first introduced for surface wave dispersion imaging by Luo et al. (2008). The advantage of the HRLRT approach is that it helps separate overlapping surface wave modes by improving resolution in both the frequency and velocity domains. A lot of work has gone into using HRLRT dispersion images (e.g., Luo et al. 2015). An alternative to the HRLRT was presented in Mikesell et al. (2017), whereby they frame the problem as image deblurring and avoid the need for the matrix preconditioning required by methods, such as the HRLRT. This alternative approach uses the power spectra of the Radon domain adjoint and the array response function to perform image deblurring on the MASW dispersion image. The non-negative least-squares inversion improves the resolution of surface wave dispersion images and promotes a sparse dispersion image. The algorithm is fast, the convergence occurs within tens of iterations, and the approach does not require estimation of the optimal damping parameter as in the HRLRT approach. Finally, the method is robust to random noise in the data and works well at low frequencies.

### Analysis of ambient noise data

The technique to estimate the dispersion curve of the blind Kumamoto exercise is based on cross-correlations of ambient seismic noise followed by the MASW analysis. The 1-h-long ambient signals were recorded in nested triangle arrays, each composed of seven 3-component Tokyo Sokushin, SE-321 velocimeters with a 10 s natural period and a sensitivity of 5 V/kine. The datalogger was an LS-8800 (Hakusan Corp) with 24-bit precision and a dynamic range of 128 dB recording at 200 Hz sampling frequency. The nested triangular arrays have different min and max interstation offsets (Table 1). In Step 1 we considered the apertures of KUM-S and KUM-SS too small to retrieve useful information, particularly given the KUM-S array had an overlapping aperture to the active seismic geophone array (Table 1), and therefore, it would not, in principle, offer new independent data. As we discuss later though, the inclusion of KUM-S data is relevant for the final interpretation, likely due to the difference in the source of seismic energy compared to the active source data (i.e., urban noise vs. hammer blows).

**Table 1** Data sources; passive KUM nested arrays and active seismic line minimum and maximum inter-station distances

| Array | $x_{min}$ (m) | $x_{max}$ (m) | Used in steps 1 and 4 |
|---|---|---|---|
| KUM-LL | 481 | 962 | Yes |
| KUM-M | 122 | 243 | Yes |
| KUM-SM | 39 | 78 | Yes |
| KUM-S | 10 | 20 | No |
| KUM-SS | 1 | 2 | No |
| Active | 1.5 | 34.5 | Yes |

We applied classical processing (Bensen et al. 2007) to the ambient noise data. This included for each 1-h-long signal, mean and trend removal, tapering and fourth-order Butterworth bandpass filter between 0.05 and 20 Hz, spectral whitening over that same frequency band, and one-bit signal binarization. The vertical component of ten second lag cross-correlations were then calculated and linearly stacked over the whole period to approximate the impulse response between two stations (2 h for KUM-LL, KUM-M and KUM-SM arrays). The impulse responses were then sorted by interstation distance. An example for KUM-M is presented in Fig. 1a. A passive seismic section was constructed using all 21 cross-correlation traces available. We averaged (stacked) the cross-correlation traces with similar interstation distances, disregarding azimuthal variations and thus assuming a

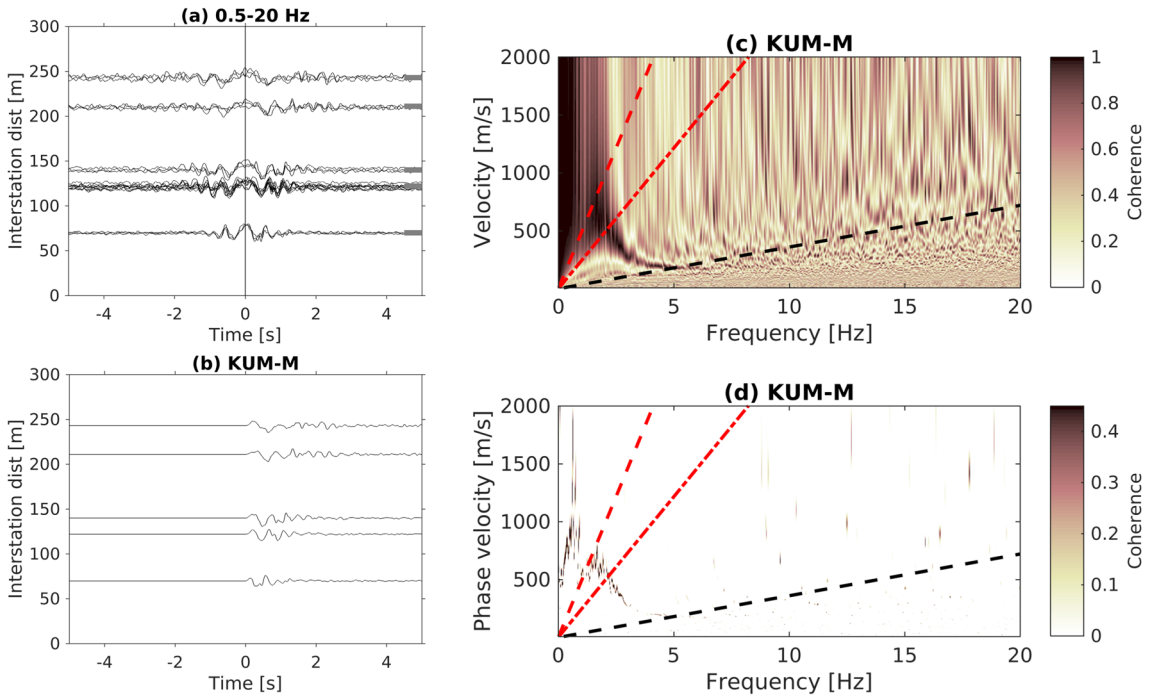


**Fig. 1** Ambient noise correlations. **a** Cross-correlations signals of the KUM-M array. **b** Binned and symmetrized cross-correlations. **c** Dispersion image from the data in **b** calculated with the (low-resolution) Radon transform. **d** The same as in **c** but calculated using the deblurring technique (Mikesell, et al. 2017). In **c** and **d,** the resolution and aliasing limits are shown by dotted and dashed straight lines, respectively

1D layered medium. Interstation distances differing by less than 10% to the mean interstation distance are considered the same, and therefore, they are binned and stacked to increase the signal-to-noise ratio. The traces are then symmetrized, meaning the negative time of the correlation is folded over and averaged with the positive time (Fig. 1b). For the case of nested triangular arrays, as used in this benchmark, there are five different interstation distances to be grouped and stacked. An example can be seen in Fig. 2 with red lines.

The surface-wave dispersion along these linearized arrays is then computed using the classical (low-resolution) Radon transform (Fig. 1c), as well as a deblurring technique (Mikesell et al. 2017) to obtain a higher resolution dispersion image of Rayleigh waves traveling across the array (Fig. 1d). Manual picking of the dispersion curves is performed on each image resulting from the KUM-LL, KUM-M and KUM-SM arrays within the resolution (maximum resolved wavelength) and aliasing (minimum resolved wavelength) limits defined by $\lambda_{max} = x_{max}/2$ and $\lambda_{min} = 2\ x_{min}$, respectively. Finally, the information is merged and interpolated by cubic splines to obtain a final broadband dispersion curve using the three ambient noise array results (Table 1) and the active seismic results (next section).

**Analysis of active seismic data**

The active-source seismic data consist of one seismic line of 24 vertical geophones (4.5 Hz natural frequency) located close to the strong motion station KUMA. The geophone spacing is 1.5 m and the maximum offset is 34.5 m and the hammer shots at each end of the line (Fig. 3). The sample frequency is 1000 Hz, and the data recording is 2 s. Classical MASW (Park et al. 1999) is carried out after stacking most of the shot gathers (Table 2). Even though we stacked multiple active-source hammer shots, the data were collected in an urban environment and not all coherent noise (e.g., automobile noise) was suppressed via stacking. High resolution dispersion images are calculated with the image deblurring technique (Mikesell et al. 2017). There is a cosine taper applied to the first and last 1% of the data before MASW. The maximum offsets of the geophone line constrain the depth of investigation to 15 m to 20 m at most (Garofalo et al. 2016). Importantly, these active-source data should allow us to characterize only the superficial soil layers, which have a strong impact on ground-motion analysis.

We note that the surface waves traveling in the two directions across the array are obviously not the same (Fig. 3) and is due to either the source or lateral heterogeneity beneath the source and the array. In addition, the

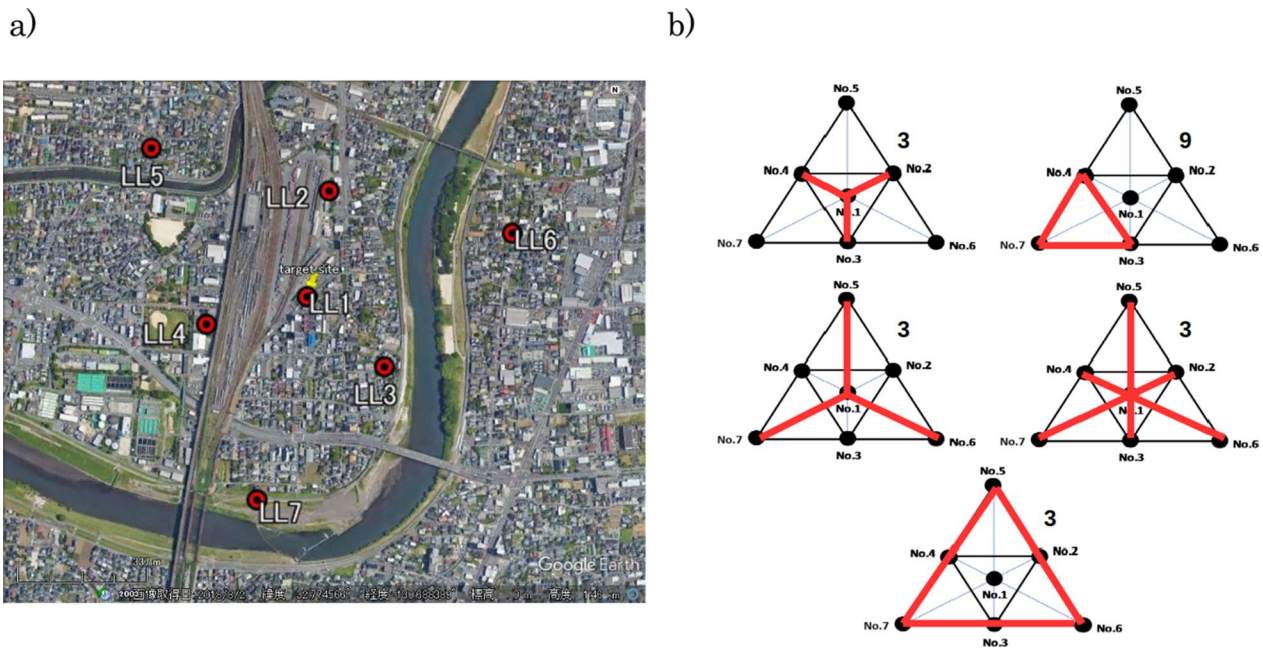


**Fig. 2** Survey geometry. **a** Stations in the KUM-LL array (red circles). The short side is 481 m, and the long side is 962 m. **b** Sampling schemes of nested-triangle arrays with the different groups of interstation distances (red colors) that are binned and stacked in this ambient noise study. On the top-right of each triangular array, the number of different interstation distance pairs is shown (i.e., 3, 9, 3, 3, and 3 for the longest path)

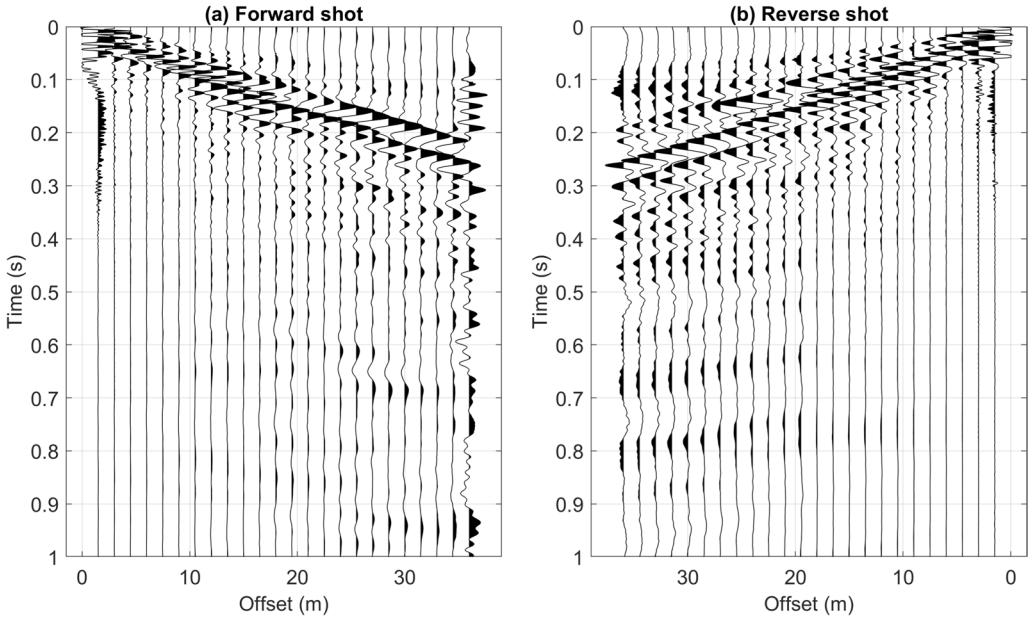


**Fig. 3** Active source data. **a** Stack of 8 sledgehammer shots in the forward direction (Table 2). **b** Stack of 9 sledgehammer shots in the reverse direction. Trace normalization is applied to enhance the surface wave arrivals at large offsets for visualization only

**Table 2** Files used; active shot files used in the stack

| Forward | Reverse |
|---|---|
| 708.txt | 720.txt |
| 709.txt | 721.txt |
| 711.txt | 724.txt |
| 712.txt | 725.txt |
| 713.txt | 726.txt |
| 714.txt | 727.txt |
| 715.txt | 728.txt |
| 716.txt | 729.txt |
| 730.txt | |

The other shots had significant urban noise

MASW results (Fig. 4) show dispersion images provide different results depending on the direction. This suggests that there may be strong lateral differences close to the surface that may be at odds with the 1D layered medium hypothesis, at least for high frequencies (> 10 Hz) and short wavelengths (< 20 m). There are obvious differences in the forward and reverse MASW images in terms of modes and lateral coherence across frequency. Thus, we needed to choose which MASW image to interpret or how to interpret both. We took the one consistent feature in both images as the fundamental mode Rayleigh wave and picked this from 17.5 to 42.9 Hz. This is the curve used in the Step-1 and Step 4 active-source component of the broadband dispersion curve. After merging several

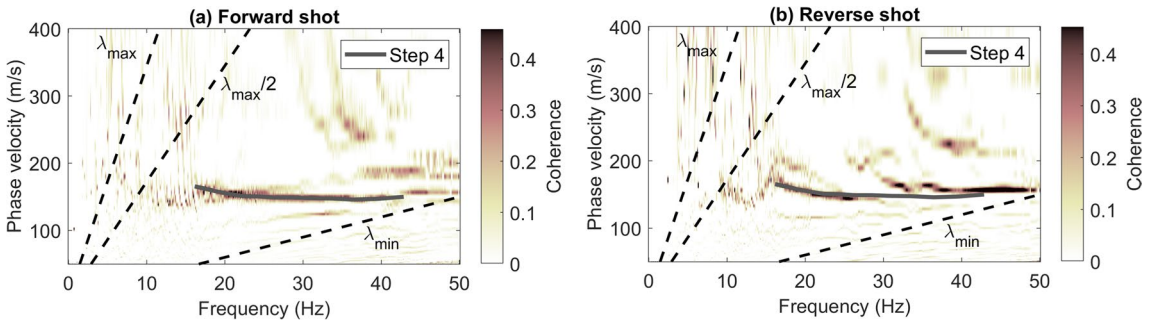


**Fig. 4** Active source MAS; high-resolution MASW images computed with the deblurring method (Mikesell et al. 2017). The Step 4 active-source dispersion curve was picked using the area, where forward and reverse shot record MASW images appeared to agree

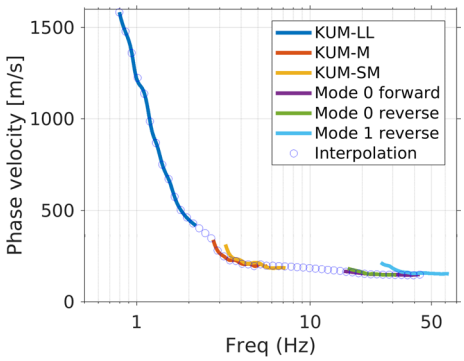


**Fig. 5** Dispersion curve; Broadband fundamental mode Rayleigh wave phase velocity dispersion curve created by combining different arrays and MASW analysis (blue dots). Small portion of higher mode energy is picked from one shot gather downline, though not used in the inversion for Step 1 and Step 4

dispersion curves from passive (KUM-LL, KUM-M, KUM-SM) and active data, a broadband Rayleigh dispersion curve from 0.9 Hz up to 45 Hz (Fig. 5) is obtained for the KUMA site. A small portion of a higher mode is picked from one shot gather downline, though it was not used for the submitted results in Step 1 and Step 4.

### Inversion of Rayleigh wave dispersion

At the end of Step 1 the organizing committee asked each participating team to submit one dispersion curve and their best inversion result (Vp and Vs profiles). At that time our Rayleigh wave phase velocity dispersion curve inversion was performed using the Neighborhood Algorithm (NA) available in the *dinver* tool, part of the Geopsy open-source software package (Wathelet et al. 2020). Assuming a 1D horizontally layered medium for the site, we performed 1D NA inversions of the broadband phase velocity dispersion curve. Since little baseline information was available within the framework of the Kumamoto blind test (Step 1), a general parameterization was used. We explored simple two-, three-, five-, and ten-layer models, but the best results came from the five-layer model of constant shear-wave velocities. Compressional wave velocities were linked to the constant shear-wave layers (to get similar layer depths for both Vp and Vs profiles) and the density was fixed at 2000 kg/m$^3$ for the sedimentary layers (first four layers) and 2200 kg/m$^3$ for the lowermost layer (volcanic bedrock). In Fig. 6, we compare our Step 1 Vs profile to the preferred model provided by the organizing ESG6 committee at the later stage (Step 4). The results are quite consistent, especially for the first hundreds of meters. Comparable values of Vs30 are found: Vs30 = 202 m/s and Vs30 = 159 m/s for the model obtained in this work and the preferred model, respectively. However, discrepancies can be clearly seen in the near-surface layers (less than 30 m) and at depths larger than 180 m. For the near surface, it is noted that the Vs values of the first layers are overestimated with respect to the preferred model. For the basin depth, considered when Vs > 1500 m/s (volcanic basement), we obtained a depth around Z = 460 m, while in the preferred model this interface is located at Z = 579 m.

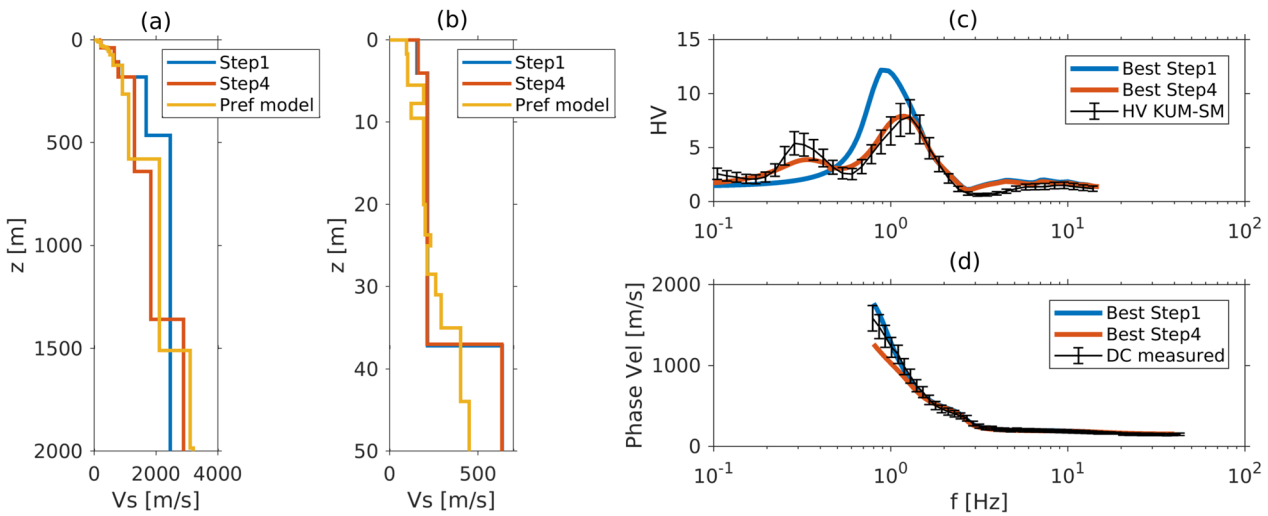


**Fig. 6** Velocity model. **a** Shear-wave velocity model for KUMA site from the inversion of the broadband fundamental mode dispersion curve (Fig. 5) for Step 1 (blue) and for Step (red) compared to the preferred model (yellow) provided by the ESG6 organizing committee for comparison. In Step 4 the HVSR data were used. **b** Zoom of the top 50 m of the shear-wave velocity model. **c** Predicted HVSR curves for the Step 1 (blue) and Step 4 (red) models, plus the HSVR data (black). **d** Predicted broadband fundamental mode dispersion curves, same color scheme as **c**

**Table 3** Velocity model; preferred model based on OYO ground investigation provided by the organizing committee

| Layer No. | Vp (m/s) | Vs (m/s) | Density (g/cm$^3$) | Thickness (m) |
|---|---|---|---|---|
| 1 | 280 | 95 | 1.5 | 1.7 |
| 2 | 490 | 100 | 1.5 | 3.8 |
| 3 | 1020 | 190 | 1.6 | 2.2 |
| 4 | 1160 | 120 | 1.5 | 1.8 |
| 5 | 1550 | 190 | 1.6 | 10.5 |
| 6 | 3470 | 200 | 1.7 | 3.7 |
| 7 | 2160 | 230 | 1.7 | 1.3 |
| 8 | 2160 | 210 | 1.7 | 3.5 |
| 9 | 1150 | 260 | 1.7 | 2.5 |
| 10 | 1440 | 290 | 1.7 | 4.0 |
| 11 | 1600 | 400 | 1.85 | 8.96 |
| 12 | 1600 | 450 | 1.85 | 11.84 |
| 13 | 1700 | 500 | 1.9 | 16.65 |
| 14 | 2100 | 600 | 1.9 | 51.07 |
| 15 | 2400 | 900 | 2.05 | 138.67 |
| 16 | 2600 | 1100 | 2.15 | 317.82 |
| 17 | 4000 | 2100 | 2.4 | 929.16 |
| 18 | 5500 | 3100 | 2.6 | 475.57 |
| 19 | 5500 | 3200 | 2.65 | – |

#### Joint inversion of mHVSR and Rayleigh wave dispersion data

After the distribution of extra information from the Kumamoto site by the organizing committee of the ESG6 blind test (Step 4) and considering that the sedimentary basin is quite deep (bedrock depth > 1 km), we decided to include mHVSR (microtremor horizontal-to-vertical spectral ratio) data calculated from the array measurements. Do this extends the usable frequency band to lower frequencies enables imaging the basin to much greater depths. We used data from KUM-LL stations, and it must be stressed that the longest resolved wavelength for dispersion analysis from the largest microtremor array KUM-LL is around 1 km and the minimum frequency is 0.8–0.9 Hz. After analysis of the mHVSR curves (Fig. 6c), a low frequency peak (around 0.3 Hz) can be clearly observed in almost all curves of the stations of each microtremor array KUM-LL, KUM-M and KUM-SM (Fig. 10). The main frequency peak that had been observed at the time of Step 1 was near 1.2 Hz. In the Step 1 inversion, data from mHVSR ratio were not available and thus was not used. The usable frequency band was 0.9–45 Hz from the broadband dispersion curve, with an estimated depth of investigation around the 300–400 m depth.

Using jointly the mHVSR curve from 0.1 to 15 Hz and the broadband Rayleigh phase velocity dispersion data, a Vs profile closer to the preferred model supplied by the ESG6 organizing committee was obtained, especially in the deeper part (> 500 m) of the model. As the results submitted for Step 1 were not far away from the preferred model, we decided to keep the first 4 layers the same, and only focus on matching the low frequency peak by including one or two deeper layers, beyond 500 m depth, to better fit the mHVSR curve (Fig. 6c). Using the HV inv code (García-Jerez et al. 2016), a global optimization is carried out by a Monte Carlo sampling technique and giving similar weights to the mHVSR and the Rayleigh phase velocity dispersion curves, a satisfactory fit is rapidly obtained. It must be noted, that the fit to the dispersion curve at low frequencies (0.8 to 1 Hz) is slightly degraded from the previous inversion of Step 1. Regardless, we decided to keep this new "best model" as the low frequency peak is now present in the mHVSR predicted data, which was not the case in the Step 1 results. This low frequency peak is related to the deepest interface (basin depth) around 1.4 km depth. The model obtained is what we submitted for as our Step 4 results to organizing committee.

#### Revisiting results after P–S logging data released

A ground structure investigation was carried out by the OYO Corporation Water and Disaster Engineering Business Division at the site KUMA from 1 to 23 November 2019. The exact location is less than 10 m apart from the center of the KUM-# arrays and the active seismic line. This included PS logging from the surface down to 39 m depth at a 0.5 m depth interval. This provided P- and S-wave velocities that made up part of the preferred model (Table 3). Using the preferred model furnished by the organizers after the first results were submitted (Step 1) we computed the theoretical Rayleigh wave phase velocity dispersion curves using Herrmann (2013). We overlaid these on the forward and reverse active-source MASW dispersion images (Fig. 7). Prior to computing the MASW images we also processed the shot records more. We applied a velocity-based window operation from 50 to 600 m/s to remove energy outside this velocity window. We also removed the two nearest offsets in each direction to avoid near field effects; thus, this changes the array resolution parameter $\lambda_{max}$ to 28.5 m.

Both the revised forward and reverse MASW images indicate that the originally interpreted fundamental mode ($m_0$) is actually the 2nd overtone ($m_2$). The observation that the MASW images are not the same, especially

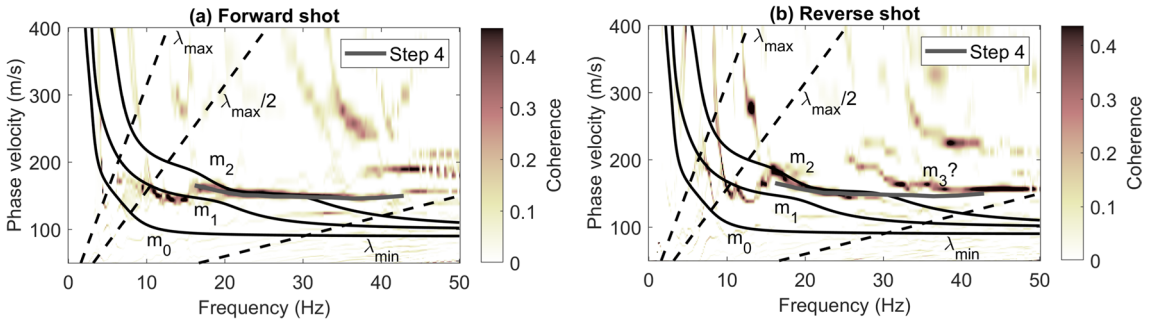


**Fig. 7** High-res MASW; Forward (**a**) and reverse (**b**) direction high-resolution MASW images computed with the deblurring method (Mikesell et al. 2017). In addition, the two near-offset traces (1.5 and 3.0 m) were removed from the shot records (Fig. 3) prior to applying the MASW. A velocity-based window is also applied to time series from 50 to 600 m/s to remove energy outside this velocity range prior to MASW. Solid curves are predicted modes for "preferred model" (Table 3)

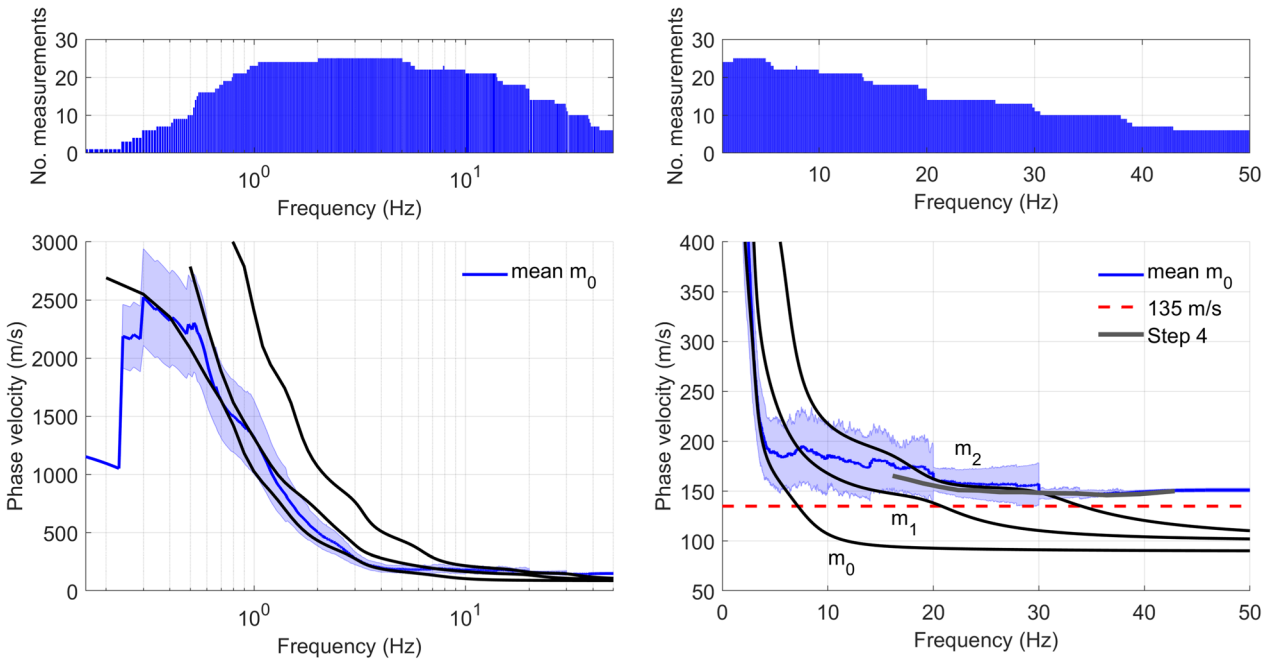


**Fig. 8** Blind test summary; Comparison of the theoretical dispersion curves for the preferred model and the mean dispersion curve from all submitted data to this blind experiment

regarding the location of modal energy is a direct result of the lateral variation beneath the source and array. In the forward direction the first and second higher modes are excited, but not the fundamental mode. Interestingly, the modes are not excited with the same energy in the reverse direction (e.g., the weak $m_1$ in the reverse direction) and it appears that a 3rd overtone is excited in the reverse direction ($m_0$). Furthermore, above the $\lambda_{max}/2$ line the modes no longer follow the predicted curves in either the forward or reverse direction.

There are a few possible reasons that the fundamental mode ($m_0$) is not observed in the active-source data. The first relies on the fact that the frequency content of the shot gathers using a sledgehammer source is concentrated from 15 to 60 Hz. At this frequency range the energy "jump" from fundamental to higher modes could have already taken place. The other is that the fundamental mode is horizontally polarized in the frequency range of the active source, and thus the energy is weakly present (or not present at all) on the vertical component

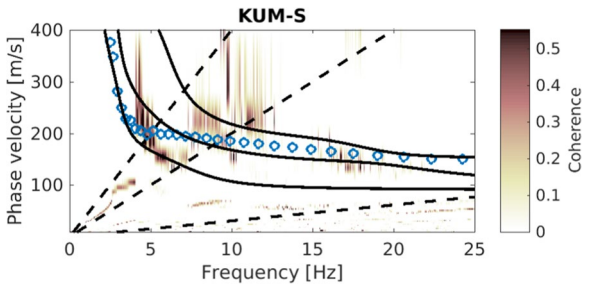


**Fig. 9** Passive MASW; Theoretical Rayleigh wave phase velocity dispersion curves (black curves) on top of KUM-S MASW image. The misinterpreted results submitted at Step 1 (blue circles) are also shown

geophones. Rayleigh waves are surface seismic waves that propagate with an elliptical motion due to the interaction of P and SV waves (Rayleigh 1885); thus, their energy is split on the vertical and radial component of a three-component geophone or seismometer. Under many geologic conditions, fundamental and higher modes can be difficult to identify, isolate, and measure (Gao et al. 2016; Ivanov et al. 2011; Dal Moro et al. 2015; Boaga et al. 2013). This case study is another example, where the use of multicomponent seismic recordings would have been quite useful to not only measure dispersive phase velocities, but also to potentially identify the modes correctly. Recording the in-line (radial) component during the active source experiment would be useful to answer this question for Rayleigh waves. In addition, the higher modes might disappear on the vertical component data, because at a certain frequency, they also become more horizontally polarized with most of their energy on the in-line component.

Given this discrepancy in our mode identification, we wanted to check how all participant teams performed in terms of mode identification. We plot the mean dispersion curve from all submissions provided by the organizing committee (Step 4) with associated standard deviations. We overlay the preferred model dispersion curves ($m_0$, $m_1$, $m_2$) and indicate the number of submitted velocity points at each frequency (Fig. 8). Considering the full frequency range (left-hand side), we see that the mean fundamental mode dispersion curve falls between the fundamental and first higher mode. For frequencies above 3 Hz we need to zoom into the plot (right-hand side). Above 3 Hz there is quite a divergence from the predicted fundamental mode, with all models departing from the fundamental mode around 7 Hz and jumping to the first overtone and then to the second overtone by around 15 Hz. Looking at the preferred model (Table 3), we see that the top 4.5 m of the model is around 100 m/s, which is the velocity that the fundamental mode has above 10 Hz. No group in this blind study submitted a velocity below 135 m/s, with the average around 150 m/s. This means the velocity in the top 4.5 m was overestimated in the best inversion by around 30% and even more if we consider the average velocity value. If we consider the low velocity layer starting at 7.7 m, the error effects even a greater portion of the important near-surface building and engineering environment.

Apart from the active source data, we also revisited the shorter array KUM-S, that had not been used in Step 1 to see if the urban noise sources excited the fundamental mode. The maximum aperture of KUM-S is on the order of the active seismic line. As we can clearly observe in Fig. 9, the fundamental mode in our submitted Step 4 results (open circles) was picked following the 2nd overtone m 2 in the active seismic data, above 17.5 Hz. This misinterpretation caused an overestimation of the shear-wave velocities of the first soil layers and consequently in the estimated Vs30 value. Interestingly, the fundamental mode was excited in the urban environment, likely by lower frequency sources. Thus, in summary, there was a complete misinterpretation of the fundamental mode at frequencies higher than 5 Hz, in not only our results, but possibly in many other participating teams. The use of both active (MASW) and passive array data (KUM-S), particularly of similar apertures, enables us to recognize and correctly identify the Rayleigh waves modes, even without using P–S logging information. In Fig. 9 the misinterpreted fundamental mode submitted at the end of Step 1 is obvious. If this dispersion image had been used at that time, the mode jump close to 7 Hz (from fundamental to 1st overtone) and at 10 Hz (from 1st to 2nd overtone) would have been more obvious, and we would have been aware of the potential for misinterpretation. In addition, we see that in the KUM-S data, the fundamental model energy is present between $\lambda_{max}/2$ and $\lambda_{max}$, but above $\lambda_{max}$ the energy does not follow the predicted fundamental mode.

## Conclusion

In this paper, we present the compelling pathway we followed during the Kumamoto blind exercise. A combination of ambient noise cross-correlation, MASW, and mHVSR techniques are used to define a shear-wave velocity profile beneath the KUMA site from the ground surface to the bottom of the deep basin of Kumamoto plain. Using ambient noise data from nested triangular arrays

of different apertures, each one composed of seven seismic stations, a broadband Rayleigh wave dispersion curve is obtained using classical cross-correlation techniques of ambient noise data. This curve is combined by classical MASW analysis of the active seismic line of vertical geophones. All MASW dispersion images are deblurred using a non-linear least square technique to facilitate the manual picking in the v–f domain. The comparison of the dispersion curve with the one calculated based on the preferred model, provided afterwards by the local ESG6 organizing committee, confirms that the results were in good agreement, at least for the first hundreds of meters. It is noted that for deeper interfaces is harder to obtain reliable results, especially due to the limited maximum array aperture (around 960 m for KUM-LL). The proposed technique demands that interstation distance must be of the order of two to three maximum wavelengths to be analyzed (in this case around 300 m maximum wavelength). This maximum wavelength limit constrains the depth penetration to image deep geological structures with only surface waves dispersion data. In addition to the broadband dispersion curve, single-station information contained in the HVSR curve was found to be useful, because a low frequency peak was present up at the site. Joint inversion of the mHVSR and the Rayleigh wave dispersion data allowed us to increase the depth penetration and image the basement unit (> 1.4 km). The possibility offered by the organizing committee to have access to the P–S logging results from a nearby borehole, allowed us to revisit the submitted results and identify the misinterpretation of higher mode Rayleigh waves as the fundamental mode. We suspect that we were not the only group to have committed the mistake. As a solution, we propose to use both active and passive multicomponent seismic data to correctly identify the surface wave modes, which may be not excited in both data sets equally or solely on the vertical component. More generally, passive seismics can be used at low frequencies (< 5 Hz), while active seismics provides energy at much higher frequencies (> 10 Hz). Finally, the natural recommendation of this exercise is to record both horizontal and vertical components in active seismic experiments to have access to the polarization of Rayleigh waves over the whole frequency band.

## Appendix

In this appendix, the microtremor HVSR curves for each station of the arrays are shown Fig. 10. They are calculated from 1 h of ambient vibrations, windows of 50 s length (Hanning taper) and Konno-Ohmachi smoothing (40%) before the spectral ratio. The mHVSR amplitude represents the mean horizontal energy. The principal peak is around 1.2 Hz at all stations, independently of the array, but a lower frequency peak is also clearly observed around 0.3 Hz.

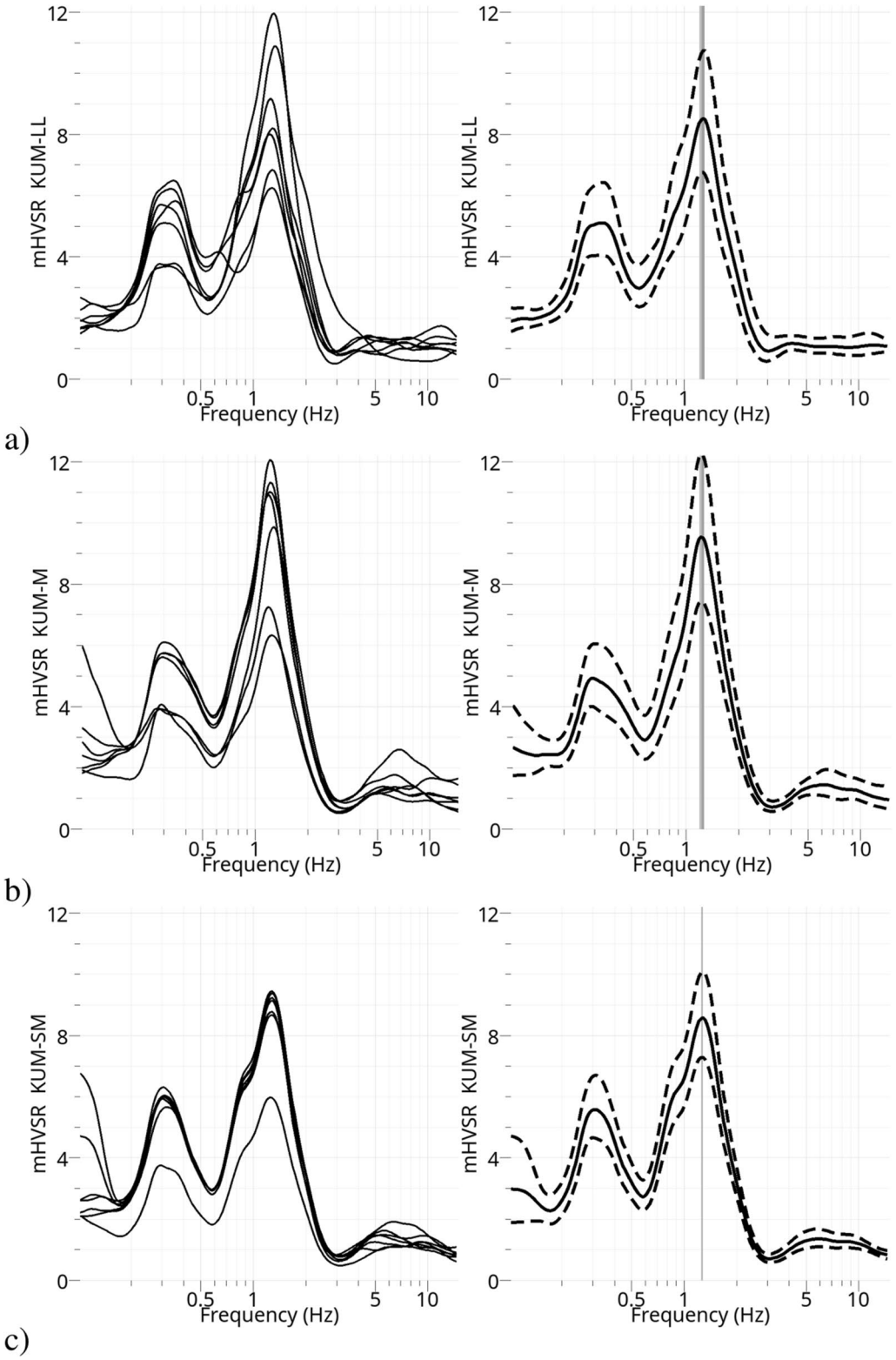


**Fig. 10** Passive mHVSR; Mean mHVSR curves at each station of the arrays KUM-LL (**a**), KUM-M (**b**) and KUM-SM (**c**). Left column: individual curves; right column: mean of each array (solid line) and one standard deviation (dashed lines)

**Abbreviations**

| | |
|---|---|
| HVSR | Horizontal-to-vertical spectral ratio |
| mHVSR | Microtremor horizontal-to-vertical spectral ratio |
| MASW | Multichannel analysis of surface waves |

**Acknowledgements**
We thank the organizers of the Kumamoto blind test, ESG6 committee.

**Author contributions**
ED Mercerat: conception, writing, data analysis. TD Mikesell: conception, writing, data analysis. Both authors read and approved the final manuscript.

**Funding**
Not applicable.

**Availability of data and materials**
Data are available upon request from the ESG6 organizing committee.

## Declarations

**Ethics approval and consent to participate**
Not applicable.

**Consent for publication**
Not applicable.

**Competing interests**
No competing interests.

**Author details**
[1]Equipe "Repsody", CEREMA Méditerranée, Sophia-Antipolis, France. [2]Natural Hazards, Norwegian Geotechnical Institute, Oslo, Norway.

Received: 17 November 2022 Accepted: 11 February 2023
Published online: 03 March 2023

**References**

Bensen GD, Ritzwoller MH, Barmin MP, Levshin AL, Lin F, Moschetti MP, Shapiro N, Yang Y (2007) Processing seismic ambient noise data to obtain reliable broad-band surface wave dispersion measurements. Geophys J Int 169:1239–1260

Boaga J, Cassiani G, Strobbia CL, Vignoli G (2013) Mode misidentification in Rayleigh waves: ellipticity as a cause and a cure. Geophysics 78:EN17–EN28. https://doi.org/10.1190/geo2012-0194.1

Chimoto K, Yamanaka H, Tsuno S, Miyake H, Yamada N (2016) Estimation of shallow S-wave velocity structure using microtremor array exploration at temporary strong motion observation stations for aftershocks of the 2016 Kumamoto earthquake. Earth Planets Space 68:1–10

Chimoto K, Yamanaka H, Tsuno S, Matsushima S (2022) Predicted results of the velocity structure at the target site of the blind prediction exercise from microtremors and surface wave method as Step-1. In: Report of the experiments for "The 6th International Symposium on Effects of Surface Geology on Seismic Motion". submitted to Earth Planets and Space

Dal Moro G, Moura RM, Moustafa SS (2015) Multi-component joint analysis of surface waves. J Appl Geophys 119:128–138. https://doi.org/10.1016/j.jappgeo.2015.05.014

Diaz J, Ruiz M, Sánchez-Pastor PS, Romero P (2017) Urban seismology: on the origin of earth vibrations within a city. Sci Reports 7:1–11

Foti S, Hollender F, Garofalo F, Albarello D, Asten M, Bard P-Y et al (2018) Guidelines for the good practice of surface wave analysis: a product of the InterPACIFIC project. Bull Earthq Eng 16:2367–2420

Gao L, Xia J, Pan Y, Xu Y (2016) Reason and condition for mode kissing in MASW method. Pure Appl Geophys 173:1627–1638

Garcia-Jerez A, Pina-Flores J, Sanchez-Sesma FJ, Luzon F, Perton M (2016) A computer code for forward calculation and inversion of the H/V spectral ratio under the diffuse field assumption. Comput Geosci 97:67–78

Garofalo F, Foti S, Hollender F, Bard PY, Cornou C, Cox BR et al (2016) InterPACIFIC project: comparison of invasive and non-invasive methods for seismic site characterization. Part I: intra-comparison of surface wave methods. Soil Dynam Earthq Eng 82:222–240. https://doi.org/10.1016/j.soildyn.2015.12.010

Herrmann RB (2013) Computer programs in seismology: an evolving tool for instruction and research. Seismol Res Lett 84:1081–1088. https://doi.org/10.1785/0220110096

Ivanov J, Miller RD, Peterie S, Zeng C, Xia J, Schwenk T (2011) Multi-channel analysis of surface waves (MASW) of models with high shear-wave velocity contrast. In: SEG Technical Program Expanded Abstracts 2011. Society of Exploration Geophysicists. pp. 1384–1390

Luo Y, Xia J, Miller RD, Xu Y, Liu J, Liu Q (2008) Rayleigh-wave dispersive energy imaging using a high-resolution linear Radon transform. Pure Appl Geophys 165:903–922. https://doi.org/10.1007/s00024-008-0338-4

Luo Y, Yang Y, Zhao K, Xu Y, Xia J (2015) Unraveling overtone interferences in Love-wave phase velocity measurements by Radon transform. Geophys J Int 203:327–333. https://doi.org/10.1093/gji/ggv300

Ma Y, Clayton RW (2016) Structure of the Los Angeles Basin from ambient noise and receiver functions. Geophys J Int 206:1645–1651

Matsushima S, Yamanaka H, Tsuno S, Chimoto K, Suzuki H, Kawase H (2022) Investigation of the subsurface structure at the target site in Kumamoto, Japan and the distributed data of the blind prediction exercise. In: Report of the experiments for "The 6th International Symposium on Effects of Surface Geology on Seismic Motion". submitted to Earth Planets and Space

Mikesell TD, Gribler G, Xu Z, Haney MM (2017) High-resolution dispersion images from deblurred MASW. In: SEG Technical Program Expanded Abstracts 2017. Society of Exploration Geophysicists. pp. 5284–5288

Pacheco D, Mercerat ED, Courboulex F, Bonilla LF, Laurendeau A, Alvarado A (2022) Profiling the Quito basin (Ecuador) using seismic ambient noise. Geophys J Int 228:1419–1437. https://doi.org/10.1093/gji/ggab408

Park CB, Miller RD, Xia J, Hunter JA, Harris JB (1999) Higher mode observation by the MASW method. In: SEG Technical Program Expanded Abstracts 1999. Society of Exploration Geophysicists. pp. 524–527

Pastén C, Sáez M, Ruiz S, Leyton F, Salomón F, Poli P (2016) Deep characterization of the Santiago Basin using HVSR and cross-correlation of ambient seismic noise. Eng Geol 55–66:201. https://doi.org/10.1016/j.enggeo.2015.12.021

Rayleigh L (1885) On waves propagated along the plane surface of an elastic solid. Proc London Math Soc s1–17:4–11. https://doi.org/10.1112/plms/s1-17.1.4

Saygin E, Cummins PR, Cipta A, Hawkins R, Pandhu R, Murjaya J et al (2016) Imaging architecture of the Jakarta Basin, Indonesia with transdimensional inversion of seismic noise. Geophys J Int 204:918–931

Shapiro NM, Campillo M, Stehly L, Ritzwoller MH (2005) High-resolution surface-wave tomography from ambient seismic noise. Science 307:1615–1618

Shen C, Wang A, Wang L, Xu Z, Cheng F (2015) Resolution equivalence of dispersion-imaging methods for noise-free high-frequency surface-wave data. J Appl Geophys 122:167–171. https://doi.org/10.1016/j.jappgeo.2015.09.019

Song Y, Castagna JP, Black RA, Knapp RW (1989). Sensitivity of near-surface shear-wave velocity determination from Rayleigh and Love waves. In: SEG, 59th Annual Meeting, Dallas, Texas, pp 509–512

Trad D, Ulrych T, Sacchi M (2003) Latest views of the sparse Radon transform. Geophysics 68:386. https://doi.org/10.1190/1.1543224

Tsuno S, Korenaga M, Okamoto K, Yamanaka H, Chimoto K, Matsushima T (2017) Local site effects in Kumamoto City revealed by the 2016 Kumamoto earthquake. Earth Planets Space 69:1–10
Vassallo M, De Matteis R, Bobbio A, Di Giulio G, Adinolfi GM, Cantore L et al (2019) Seismic noise cross-correlation in the urban area of Benevento city (Southern Italy). Geophys J Int 217:1524–1542
Wathelet M, Chatelain J-L, Cornou C, Giulio GD, Guillier B, Ohrnberger M, Savvaidis A (2020) Geopsy: a user-friendly open-source tool set for ambient vibration processing. Seismol Res Lett 91:1878–1889

## Publisher's Note